Buness *et al. Geothermal Energy* (2026) 14:33
https://doi.org/10.1186/s40517-026-00417-1

Geothermal Energy

RESEARCH Open Access

Impact of local roughness gradients on laminar flow within granite fractures

Carola M. Buness[1*], Fabian Nitschke[1] and Thomas Kohl[1]

*Correspondence:
Carola M. Buness
carola.buness@kit.edu
[1]Geothermal Energy and Reservoir Technology, Institute of Applied Geosciences, Karlsruhe Institute of Technology, Kaiserstraße 12, Karlsruhe 76131, Germany

Abstract
Accurately predicting fluid dynamics in crystalline rock remains fundamental to deep geothermal reservoir management. In particular, within the wider pressure-stimulated zones of geothermal reservoirs, high fluid pressures drive low effective normal stress conditions, often resulting in normal opening or shear displacement with minimal abrasion. This study investigates the relationship between granitic fracture roughness and the resulting flow behavior under these conditions. While global surface statistics are frequently used to characterize fractures, this study investigates whether local topography fluctuations are a more critical factor. We conducted high-resolution topography measurements of granite fracture samples from three locations next to the geothermal anomaly of the Rhine Graben. Our analysis reveals that local fluctuations in the roughness height gradient dominate the evolution of the fracture aperture during shear. The resulting fracture voids exhibit mean apertures up to 2 mm larger than conventional models suggest, leading to a decreased normalized local aperture distribution, widening with shear distance. To quantify the fluid dynamic impact of these geometric shifts, we employed a dual-modeling approach applying laminar flow at low Reynolds numbers: a 1D model was used to isolate how the width of the aperture distribution affects the fracture hydraulics, while a 3D model investigated how the overall aperture increase governs the flow direction. Our results demonstrate that the local height gradients of natural fracture surfaces significantly increase hydraulic conductivity by expanding the mean aperture. However, an aperture distribution width of 18% (e.g. introduced by fracture shearing) leads to a pressure increase of above 25% compared to a parallel plate assumption. Furthermore, the increased aperture in sheared fractures was found to reduce spatial flow non-uniformity. These findings suggest that conventional models should be expanded beyond global statistics to integrate the geometrical effects of natural, extreme local height gradients by increasing the fracture mean aperture.

Keywords Enhanced geothermal systems (EGS), Self-affine surfaces, Hydraulic conductivity

Introduction

Deep geothermal systems have considerable potential to expand the contribution of geothermal energy by providing a reliable, low-carbon baseload supply of heat and electricity. However, this potential can only be leveraged under favorable hydraulic reservoir

© The Author(s) 2026. **Open Access** This article is licensed under a Creative Commons Attribution 4.0 International License, which permits use, sharing, adaptation, distribution and reproduction in any medium or format, as long as you give appropriate credit to the original author(s) and the source, provide a link to the Creative Commons licence, and indicate if changes were made. The images or other third party material in this article are included in the article's Creative Commons licence, unless indicated otherwise in a credit line to the material. If material is not included in the article's Creative Commons licence and your intended use is not permitted by statutory regulation or exceeds the permitted use, you will need to obtain permission directly from the copyright holder. To view a copy of this licence, visit http://creativecommons.org/licenses/by/4.0/.

conditions, which ultimately control geothermal system performance. In this context, reservoir performance is defined by the ability to sustain high production and injection rates at low required pressure gradients. The performance of geothermal reservoirs is therefore highly sensitive to their hydraulic transmissivity which governs the flow rates that can be sustained for a given pressure gradient and therefore directly controls reservoir productivity and injectivity. In contrast to reservoirs in matrix-porous host rocks, the transmissivity of crystalline basement reservoirs is primarily controlled by fracture networks and, at the smallest scale, by fluid flow within individual fractures. Consequently, the strong dependence of geothermal system performance on fracture-controlled hydraulics requires a robust and comprehensive understanding of fluid flow within individual fractures. This direct coupling between fracture-scale physics and system-scale response highlights that reliable prediction and successful exploitation of geothermal reservoirs critically depend on a detailed and quantitative understanding of the governing physical mechanisms and their parameter sensitivities. One important physical mechanism is channeling, where preferential flow paths form due to complex fracture void geometry. In the literature, flow channeling is frequently investigated, though its definition remains inconsistent across studies. Quantification of channeling strength typically relies on a threshold, resulting in a binary classification of the fracture into 'channel' and 'non-channel' areas. Examples include the use of a 90% flow rate threshold (Cardona et al. 2021) or a flow rate ratio threshold of 0.33 (Egert et al. 2023), highlighting that a universally applicable, physically based criterion is still lacking. Despite these varying operational definitions, models consistently show that channeling strongly depends on fracture aperture and shear (Marchand et al. 2020). Stronger channeling reduces fluid interaction with the fracture surface, thereby lowering the heat-extraction efficiency (Chen and Zhao 2020). Consequently, accurately predicting channeling behavior requires numerical and experimental characterization of the fracture void space.

The reliability of these investigations, depends on the specific methodologies used to characterize the fracture apertures. Therefore, two conceptual models are frequently encountered in the literature to define fracture apertures: (1) the one-contact-point model, where the surfaces roughness remains intact and shear displacement leads to the fracture dilation governed by a single point of contact, which defines the average fracture aperture (Auradou et al. 2006; Marchand et al. 2020; Egert et al. 2021) and (2) the contact-area model, which numerically allows the opposing surfaces to interpenetrate while simulating physical asperity deformation or break offs under load. Here, the fracture aperture is often defined by the amount of overlapping contact area (Park and Song 2013; Finenko and Konietzky 2024). This area is based on fracture normal stress and rock stiffness or defined directly from contact area measurements (Re and Scavia 1999). While the necessary rock stiffness parameter is naturally given in experimental settings using rocks in triaxial cells (Hofmann et al. 2016), this parameter must be defined for simulations. Due to the lack of reliable rock normal and shear stiffness data on the resolution of individual mineral components, simulations often set different contact area ratios (Li et al. 2026a). This contact-area model is more reliable at high normal stress (Nemoto et al. 2009) whereas the one-contact-point model is applicable for low normal effective stress conditions, which occur especially near geothermal injection wells (Zeng et al. 2018) and wider pressure-stimulated zones. In both aperture models, the roughness is crucial for determining the resulting fracture aperture. This roughness is typically

parameterized using global roughness metrics such as the Hurst Exponent (Schmittbuhl et al. 1993) or the height standard deviation (Rong et al. 2021). These global parameters provide single values to describe the fracture roughness.

In recent years, studies have begun investigating local deviations from the global roughness descriptions. Zhu and Yu (2024) measured and simulated the transport properties of fractured shales under normal stress, finding the hydraulics controlled by narrow points within flow channels, describing them as bottlenecks. While these insights are valuable from a fluid dynamics perspective, the authors attribute this narrowing partly to clay swelling. Consequently, these specific findings cannot be directly extrapolated to crystalline fractures, where such swelling mechanisms are absent. A more theoretical study by Li et al. (2026b) investigated the influence of local aperture reduction by simulating 2D fracture flow, focusing on the non-linear hydraulic regime. In their model, aperture reduction was modeled by adding local roughness steps to granite scans, allowing them to control step extent and quantity. Their findings show that these local aperture reductions enhance the non-linear hydraulics by creating large-scale (dead) recirculation zones downstream. In the analysis of fracture flow within crystalline reservoirs, a critical knowledge gap remains: the proof of the occurrence of local roughness steps and their impact on linear hydraulics. To address this gap of analyzing local roughness steps and their extent for crystalline formations, this study investigates the hydraulic significance of observed local roughness extrema. First, the occurrence of local roughness gradient extrema by comparing high-resolution measurements of physical fracture surfaces with simulated rough surfaces is examined. Second, since these extrema control the evolution of fracture void geometries, a more accurate basis for hydraulic predictions is assessed. In a final step, we evaluate the impact of these geometric variations on fluid flow at low flow rates to determine how these local features fundamentally alter hydraulics even within the linear hydraulic regime. Through hydraulic modeling and local flow direction analysis, this study suggests a more naturally representative framework for predicting reservoir hydraulics.

Methods

The impact of local roughness extrema on laminar fracture flow was examined by the workflow illustrated in Fig. 1. As a starting point, we scanned and characterized a diverse topographical dataset of three distinct rock samples to investigate the natural occurrence, and three additional simulated self-affine rough surfaces to compare with numerical studies. To ensure comparability with previous literature, we characterized all surface topographies using the following global and local metrics: Global roughness was quantified using power spectral density (PSD), Hurst exponent H, and standard deviation of height σ_z. Local roughness was defined by the height gradient ∇z. Two conceptual models were applied to theoretically represent the fracture void space under different normal stress conditions and to derive the corresponding local and average apertures. Based on the results, two numerical laminar fracture flow simulations were performed: A 1D approach was used to analyze the effect of the local aperture distribution width in isolation, while the impact of variations in the mean aperture on flow uniformity was assessed using a 3D flow simulation to capture the local flow direction in all spatial dimensions.

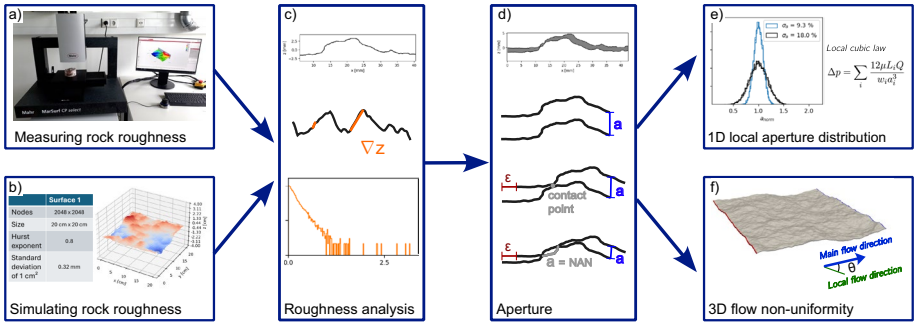


Fig. 1 Flowchart of the investigation of the influence of local rock roughness on fracture flow: Starting from roughness measurements of fracture surfaces **(a)** and simulations of self-affine surfaces **(b)**, we analyzed global and the local height gradient as the local roughness parameter **(c)**. The resulting aperture was modeled for all surfaces using the one-contact-point and the contact-area model **(d)**. Based on the findings of the aperture analysis, the influence on laminar fracture flow is investigated first with a 1D model to investigate the influence of the aperture distribution width **(e)** and second with a 3D model for the spatial flow non-uniformity for different fracture apertures **(f)**

Rock roughness

Characterizing natural roughness and comparing it against our simulated roughness serves as the foundation for the geometric fracture model. To capture the geological diversity of crystalline geothermal reservoir rocks, we selected three granite fracture surfaces representing different fracture mechanisms and degree of alteration. This diversity ensures that the identified local roughness extrema are not an artifact of one specific sample but instead represent characteristics of granitic fractures more broadly, supporting the generalizability of the findings. Three different granitic fracture surfaces were measured: (1) a joint-type surface from cored geothermal wells from Soultz-sous-Forêts, France, characterized by a macroscopically fresh fracture surface and inhomogeneous grain size (surface 1); (2) a Malsburger Granite, with uniform medium- to fine-crystalline grain texture, fractured under controlled laboratory conditions within a triaxial cell (surface 2); (3) an altered granite with a fracture surface, coated with secondary material, from the cored GLB01 borehole of the Tromm Massif, Germany, (surface 3). Utilizing a Soultz-sous-Forêts sample ensures the roughness profiles directly represent operational Enhanced Geothermal System targets. Incorporating the surface 2 enables the characterization of pure mechanically induced topography. Meanwhile, the surface 3, sourced from a planned GeoLaB site, accounts for the geochemical history typical of deep reservoirs, where mineralization alters primary fracture topographies. The three surfaces were scanned with a resolution of 30 µm × 30 µm using an optical 2D profilometer (Mahr, MarSurf CP select) with a vertical resolution of 0.3 µm. Photos of the rock samples, including the scan areas, are presented in Fig. 2.

While these physical samples provide geological realism, their fixed properties prevent isolating the influence of individual parameters. Therefore, to compare the natural properties with simulated roughness used in systematic studies (Marchand et al. 2020), we complemented the rock surfaces with three simulated, self-affine surfaces using the software *SAFFT*, developed by Méheust and Schmittbuhl (2001), and *TAMAAS*, by Frérot et al. (2020). As a definition of roughness and its scaling behavior, the Hurst Exponent H was used. In accordance with H measurements by Candela et al. (2012) for fault roughness in the slip direction and normal to the slip direction, H was set to 0.8 for both software simulations, resulting in the surfaces named gen. surface 1 and gen.

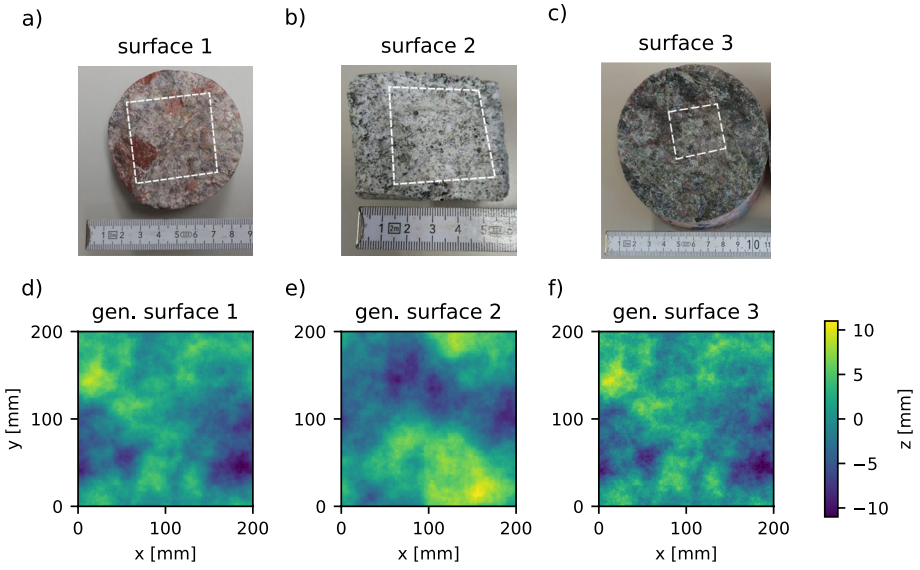


Fig. 2 Used roughness samples: Photos of the measured fracture surfaces **(a–c)** with indicated scanned areas (white line) of three different granite roughness samples and height profiles of the simulated rough surfaces **(d–f)** defined by two different Hurst exponents *H* and simulated by two different software

surface 2. Additionally, H was set to 0.6 for the third surface named gen. surface 3, simulated with *SAFFT*. The surfaces, consisting of 2048×2048 nodes, were scaled to dimensions of 20 cm × 20 cm. The height scaling for the simulated surfaces with $H = 0.8$ was adopted from the surface 1 height by using the average of the height standard deviation of 10 mm^2 sub-areas ($\sigma_z(10mm^2) = 0.32$ mm), as described in Buness et al. (2026). The roughness height of the simulated surface with $H = 0.6$ was adjusted to match the standard deviation of the whole gen. surface 1 $\sigma_{z,tot}$.

All six surfaces were analyzed using standard global roughness parameters (PSD, H, σ_z). Prior to statistical analysis, the measured surfaces were rotated so that the mean surface plane aligned with the x-y-plane. The 1D Power Spectral Density (PSD) was calculated (using the function *periodogram* from the *scipy* python library) along the grid directions as the mean over all data rows. H was determined by a 1D rescaled range (R/S) analysis (Mottl 2019). In this approach, H is extracted via a linear fit of the R/S data over n with $R(n)/S(n) = C \cdot n^H$. In this approach, the full 1D height-profile line is divided into multiple non-overlapping windows $\tau_{1D,i}$, each consisting of n data points. For each scale n, the ratio $R(n)/S(n)$ with $S(n)$ the standard deviation and $R(n)$ the maximal difference of the cumulative sum of the height deviation from the mean value within $\tau_{1D,i}$, is calculated for each i-th segment and then averaged across the entire line. By varying n over a broad range of window sizes, H is determined as the slope of the resulting linear fit in a double log plot, additionally having C as a constant. To account for the anisotropy of the rough surfaces, this analysis was repeated for 34 equally spaced directional angles γ with multiple parallel lines spaced 3 mm apart for each angle. Angles deviating from the original grid were calculated via a linear interpolation between the measured points. Due to the random x-y orientation of the measured data, all resulting $H(\gamma)$ datasets were rotated to align the lowest calculated H with the arbitrary zero-degree angle for comparison.

For the height parameter, the height standard deviation σ_z was used. Since measured rock surfaces are known to be self-affine (Schmittbuhl et al. 1993), σ_z for the entire

surface is reliable only if all compared surfaces share the same surface area. To address this, we analyzed the standard deviation of height σ_z of smaller sub-areas τ_{2D}, orders of magnitude smaller than the whole measured surface. A moving-window approach was employed to cover the entire surface with these τ_{2D}. The resulting σ_z for each τ_{2D} size is the arithmetic mean of all analyzed τ_{2D} of that size. The τ_{2D} size was varied from 10×10 data points up to one-quarter of the total surface area.

As a local roughness parameter, we used the absolute local roughness height gradient $\nabla z = |\frac{\Delta z}{\Delta x}|$. This was calculated along the measurement grid axes along x over a specified distance Δx. By varying Δx from 1 to 100 points, we investigated the resolution characteristics of self-affine local roughness. To facilitate comparison between the measured and simulated surfaces, a consistent area of 9 cm^2 was analyzed for each surface. This local topographical characterization provides the geometric analysis for the subsequent construction of the fracture void spaces based on these roughness samples.

Fracture aperture

To translate individual surface topographies into hydraulic properties, the geometry of the fracture void must be accurately represented. In the literature, this fracture void is quantified using several definitions for the aperture a, ranging from the effective aperture, measured perpendicular to the local slope (Marchand et al. 2020), to the hydraulic aperture a_h, back-calculated from flow measurements (Li et al. 2026a). While a detailed comparison of these definitions is beyond the scope of this study, we define the local fracture aperture a as the distance in the z-direction, perpendicular to the mean fracture surface plane, which allows it to be derived directly from the roughness. The average fracture aperture $\bar{a}$ is defined as the arithmetic mean of a. To calculate the fracture void, the two identical fracture surfaces are kept in a parallel configuration. The three applied models are sketched in Fig. 1: For normal opening, the top surface is just elevated to the defined $\bar{a}$. Under shear conditions, the one-contact-point model is primarily applied, where the fracture aperture is determined by a single point of contact between the surfaces (i. e. $min(a) = 0$). In the contact-area model, the confining surfaces interpenetrate until the contact area corresponds to a requested percentage. The contact areas were calculated ranging from a single point up to 20%. Following the method of Cardona et al. (2021), the points of the contact area were removed for subsequent fracture void aperture calculations. The results of the void geometries serve as the basis for the hydraulic simulations required to evaluate the impact of local roughness extrema.

Flow simulation

The goal of the flow simulations was to decouple the effects of aperture distribution width from the influence of mean aperture on the fracture hydraulic and spatial flow non-uniformity. By investigating these parameters separately, we can determine the extent to which local height gradients control the fracture flow. To achieve this, we implemented a dual-modeling strategy. 1D simulations were utilized to segregate the hydraulic influence of the aperture distribution width, followed by 3D fracture flow simulations to investigate how the overall aperture increase governs the three-dimensional flow field.

For both modeling approaches, we assume laminar flow, characterized by low Reynolds numbers $Re \leq 2.8$, which dominates the far-field of geothermal reservoirs. Although

turbulent flow can occur near injection wells due to high fluid velocities, the vast majority of the reservoir volume operates under low-velocity conditions. However, already around $Re \approx 1$, the flow can get slightly non-linear due to streamline curvature (Zimmerman and Paluszny 2024). Here, Re is defined as $Re = \bar{u} \cdot \bar{a}/\nu$ where $\nu = 1$ mm²/s is the applied kinematic viscosity of water at room temperature and $\bar{u}$ is the average flow velocity as $\bar{u} = Q/(\bar{a} * w)$. The flow simulations were divided into two cases: the 1D Local Cubic Law (LCL) simulation and the 3D flow simulation using *OpenFOAM*.

The 1D simulation was calculated by the LCL

$$\Delta p = \sum_i \frac{12 \mu L_i Q}{w_i a_i^3} \tag{1}$$

where Δp is the pressure difference across the entire 1D fracture, μ is the dynamic viscosity of water ($\mu = 1$ mPa s), Q is the volumetric flow rate, a_i is the local aperture of one fracture element, L_i is the length and w_i is the pseudo-width of the fracture element. While Q, L_i, w_i were kept constant for all fracture elements, a_i was selected randomly from a normal distribution with a specified $\bar{a}$ and standard deviation σ_a. To represent the whole a distribution, the total fracture length of 0.2 m was divided into 10 000 fracture elements with $w_i = 0.2$ m, $Q = 2$ L/h and varying a_i.

The 3D fracture flow simulation is based on the open-source software *OpenFOAM*, applying a laminar, steady-state model with the SIMPLE algorithm for incompressible fluids using the GAMG solver. The fracture void mesh is based on a 128 × 128 nodes *SAFFT* ($H = 0.8$) surface with the same scaling as the gen. surface 1. The void space between the identical surfaces is defined by a specific $\bar{a}$ and shear displacement ϵ. The mesh was generated using *blockMesh*, provided by *OpenFOAM*, by refining the x-y grid spacing by half and the void height to 20 cells. Mesh refinement near the fracture walls was achieved via z-axis cell grading, using expansion ratios of 5 and 0.2 for the bottom and top 10 cells. The surface faces in the x-direction are defined as inlet and outlet (Fig. 3), while the other sides are defined as fracture walls with a no-slip velocity condition and zero pressure gradient. The pressure at the outlet is fixed at zero with a zero gradient flow velocity, while at the inlet, the velocity is fixed to a specific mean value, and the pressure is defined by a zero gradient. Numerical convergence was monitored through the evolution of the residuals for pressure and velocity components, achieving a reduction of minimum three orders of magnitude with final residuals dropping below 10^{-5}.

From the simulation results, the flow direction angle θ was calculated for each node in the x-y-plane by

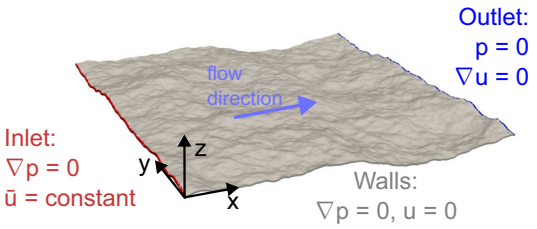


Fig. 3 The fracture model for the 3D approach with the applied boundary conditions: Inlet ($x = 0$), Outlet ($x = maximum(x)$) and Wall (all others). Additionally indicated, the main flow direction along x

$$\theta_i = arctan\left(\frac{\sum_j u_{y,i} \cdot V_j}{\sum_j u_{x,j} \cdot V_j}\right) \tag{2}$$

where $u_{x,j}$ and $u_{y,j}$ are the flow velocities in x, y direction for each cell, V_j is the corresponding cell volume, and $\sum_j$ represents the summation over all cells within the fracture. For fracture realizations with shear, a mean $\theta \neq 0$ can occur due to nonuniform inlet and outlet apertures along the y-axis. Therefore, we described the spatial flow nonuniformity by the standard deviation of the flow direction

$$\sigma_\theta = \sqrt{\frac{\sum_i (\theta_i - \bar{\theta})^2}{N-1}} \tag{3}$$

with N the number of nodes in the x-y-plane. This σ_θ provides a quantitative measure of the flow direction deviation. From a physical transport perspective, σ_θ serves as a direct statistical proxy for hydraulic tortuosity. A wider distribution σ_θ necessitates that fluid streams are continuously forced to deviate from the main flow direction, thereby increasing the actual flow path length. This parameter completes the analytical framework required to assess the impact of fracture roughness extrema on the flow. With this methodology established, the following chapter presents the results of the roughness analysis and discusses their direct consequences on fracture void evolution and fluid dynamics.

Results and discussion

Fracture roughness

The results are structured to begin with the characterization of the selected granite and simulated surfaces to confirm their self-affine behavior. This analysis serves to quantify the inherent variety within rock roughness, ensuring that the samples are representative of the granitic rock fracture diversity in deep geothermal research. All six surfaces, the three scanned fracture surfaces and the three simulated rough surfaces, were analyzed with respect to the global roughness parameters: Power Spectral Density *PSD*, the anisotropic Hurst Exponent $H(\gamma)$ and area-dependent height standard deviation σ_z. The mean *PSD* along x and y is visualized in Fig. 4a. The linearity of the *PSD* in the double logarithmic plot confirms the self-affinity of all surfaces, following the self-affine power-law scaling where roughness amplitudes increase at lower wave numbers. Furthermore, the varying slopes across the samples reflect different H values, providing the first indication of the morphological diversity within the dataset.

The analysis of H over the evaluated directions γ (Fig. 4b) highlights the differences between the surfaces. The average standard deviation of H within one γ is 0.05. While H of the simulated surfaces as well as the surface 1 vary less than the variation within a single γ, the surface 3 exhibited a slight anisotropy of 0.08 variation in H, and the surface 2 showed a more pronounced anisotropy of 0.14. According to Candela et al. (2012), the anisotropy of H is driven by shear under normal load. In this context, the observed spectrum of anisotropy quantifies the structural variety of the physical samples, capturing the transition from near-isotropic to sheared textures. The variation in H is slightly lower than the resulting mean shear-induced differences reported by Candela. This discrepancy may stem from a smaller shear displacement in the presented samples compared to the faults measured by Candela or from differing mechanical rock properties, which

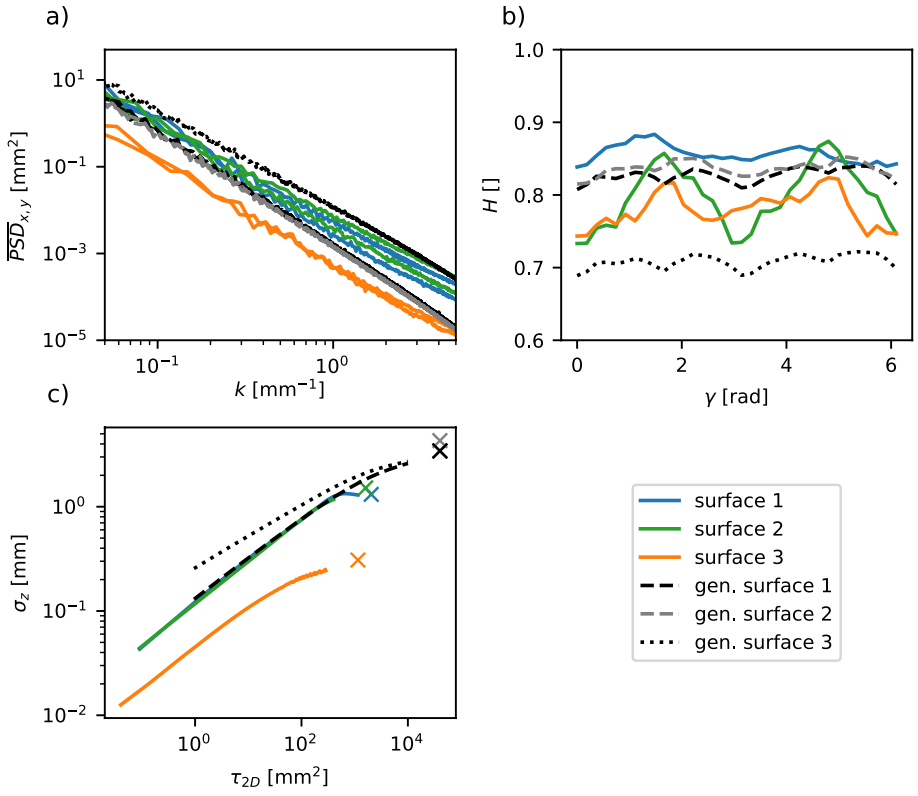


Fig. 4 Global rock roughness analysis of all six roughness samples: The power spectral density (PSD) over the wavenumber k showing the self-affinity of all surfaces **(a)**, the angle γ dependent Hurst exponent (H) for the anisotropy analysis **(b)** and the height analysis by the height standard deviation σ_z over different sub-area sizes τ_{2D} for the full roughness height description **(c)**

are out of scope at this point. The slight, regular variation in H for the simulated surfaces is an artifact from linear interpolation for angles differing from the x-y measurement/simulation grid directions. This interpolation effectively smooths the surface asperities at high wave numbers and consequently yields higher H values for angles between the principal grid axes.

The height analysis (Fig. 4c) further quantifies the diversity in roughness magnitude across the dataset. It reveals that the measured surfaces of the surface 1 and the surface 2 are highly similar. The generated surfaces 1 and 2, based on σ_z of the sub-areas $\tau_{2D} = 1$ mm^2 of the surface 1, follow the linear part of the afore mentioned sample. The total $\sigma_{z,tot}$ for the entire surface is 2.6 times larger due to the 19.6 times larger surface area with the self-affine scaling of the roughness. The generated surface 3 shares the same $\sigma_{z,tot}$ as the gen. surface 1, which results in a higher σ_z at smaller τ_{2D} scales, leading to a 1.2 times larger σ_z at τ_{2D} =0.955 mm^2. The measured, surface 3 shows a significantly lower σ_z across all τ_{2D} sizes. This may be attributed to either the large-scale stress field in the Tromm Massif and subsequent large-scale shearing or the alteration of the fracture. Both hypotheses are subjects of ongoing research (Amitrano and Schmittbuhl 2002; Deng et al. 2018; Beeler 2023), and their specific impacts on fracture roughness are not yet fully understood.

Overall, the global parameters align well with existing literature regarding the self-affinity of rock fracture surfaces (Schmittbuhl et al. 1993) and their anisotropy (Candela et al. 2012). Roughness height values are difficult to compare directly with literature

data due to varying specified parameters and the common use of single data points for total roughness. However, we utilized the measured roughness height of a sub-window to calibrate the simulated surfaces, resulting in realistic roughness heights, representing the measured case. By quantifying the surface variety in H, anisotropy, and roughness height, we provide the necessary context to indicate that the local roughness extrema are a universal feature and not restricted to specific surface types.

The roughness parameter ∇z characterizes the local roughness. The distribution of ∇z for all six surfaces is shown in Fig. 5 at a resolution of $\Delta x = 0.3$ mm on a rectangular area

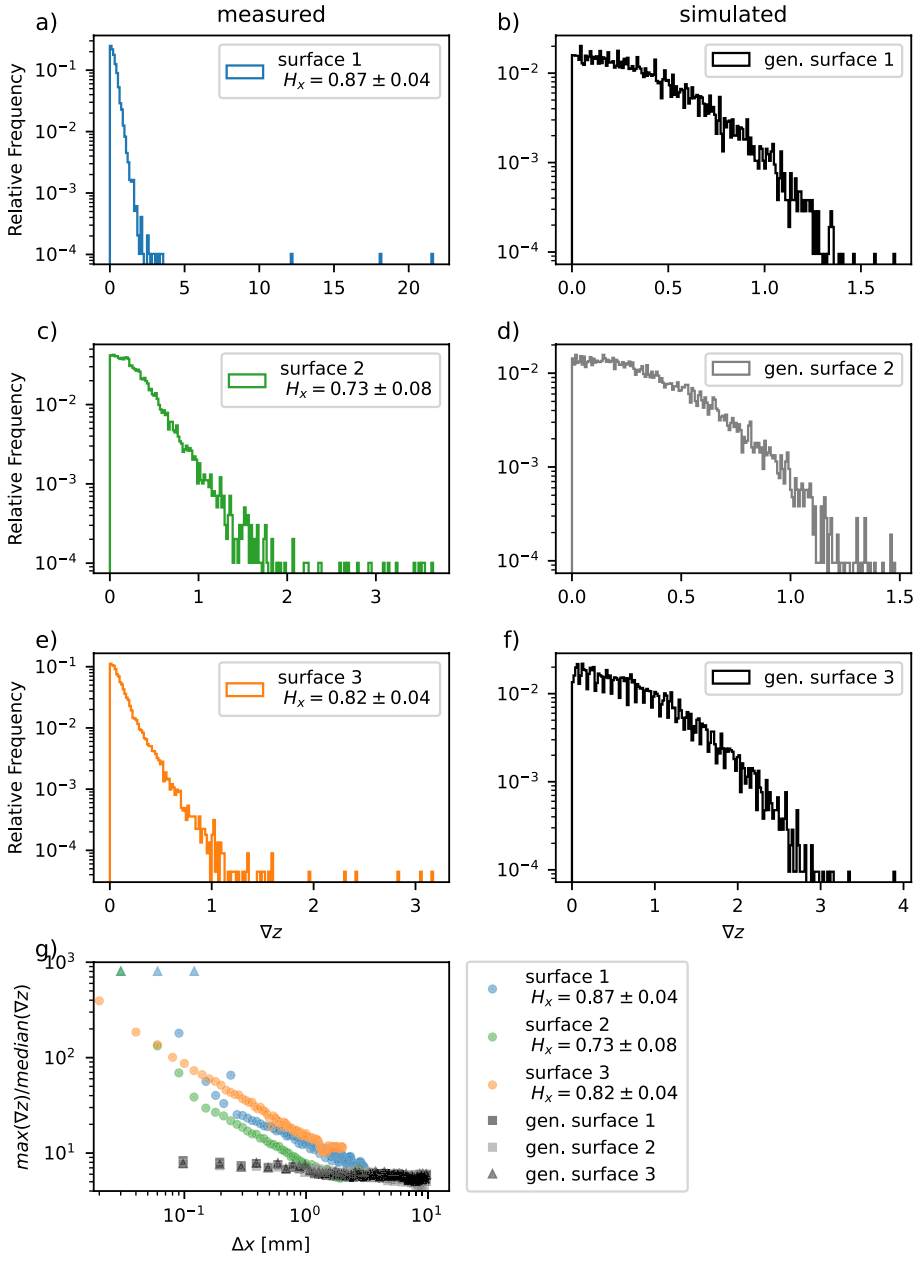


Fig. 5 Histograms of the local roughness parameter ∇z for all 6 surfaces (measured surfaces: a,c,e and simulated surfaces: b, d, f) with a resolution of $\Delta x = 0.3$ mm **(a–f)**. Additionally, the ratio of the maximum ∇z divided by the median ∇z over different grid resolutions Δx**(g)**. The black and grey marker overlay each other. The blue/green triangle-markers indicate outliers of the joint-type surface (ratios with increasing Δx: $1.4 \cdot 10^5$, $6.3 \cdot 10^4$, $1.1 \cdot 10^3$) and the surface 2 ($6.9 \cdot 10^3$)

of 9 cm^2. Two distinct observations can be made from these data: First, the measured samples exhibit a more linear distribution compared to the more downward-curving shape of the simulated surfaces ∇z distribution; second, the high ∇z extrema are significantly more pronounced in the measured surfaces. While a detailed discussion of the distribution shapes is beyond the scope of this study, we will focus on the ∇z extrema. Since the ∇z of self-affine surfaces is resolution-dependent, the ratio of the maximum ∇z to the median ∇z was analyzed across different resolutions Δx (Fig. 5g). The results demonstrate that, beyond some fluctuations at the highest resolution (low Δx), the ratio decreases linearly for all surfaces. All simulated surfaces show a similar, slight decrease. Though, the measured surfaces exhibit a much sharper decline, starting with over one order of magnitude higher ratios and decreasing to values comparable to the simulated surfaces within the measured range. This shows that the observed local roughness extrema are not a micro-scale phenomenon and occur on all measured surfaces, even on the relatively smooth surface 3.

These findings demonstrate that the use of simulated surfaces leads to an underestimation of roughness extrema. This discrepancy highlights the importance of incorporating high-resolution natural scans to complement pure mathematical studies. While a broader sample set would refine the quantitative magnitude of this effect, our results suggest that pronounced ∇z extrema are a universal characteristic of natural fractures that persists across all investigated morphologies. The same results were found by additional 15 granite fracture and two sandstone fracture measurements (Appendix A). Local roughness disturbances can exert a significant influence on fracture flow. For instance, 2D simulations demonstrated that a single local aperture reduction extent of 0.9 can reduce the hydraulic aperture to one-third of its original value (Li et al. 2026b). Accordingly, the following section focuses on these naturally occurring ∇z extrema impact on the fracture void geometry and, consequently, on the flow within these geometries.

Influence of local topography on fracture void geometry

To determine how the previously identified roughness extrema result in saturated fracture voids, we first applied the one-contact-point model to the surfaces and subsequently the contact-area model. This approach allows for a direct comparison between the void structure of natural and simulated fractures. The resulting local apertures a were then statistically evaluated, to identify the void characteristics. This analysis is visualized in detail for the measured surface 1 and the generated surface 1 in Fig. 6a–d. For these surfaces, both the a distribution and the normalized $\hat{a} = a/\bar{a}$ distribution are shown for $\epsilon \leq 2$ mm. While a follows a normal distribution in all cases, the evolution of $\bar{a}$ reveals a contrast. For the simulated surface, $\bar{a}$ increases steadily with increasing shear from $\bar{a} = 0.21$ mm up to 2.42 mm. In contrast, the aperture of the measured surface increases abruptly to $\bar{a} = 2.10$ mm with only 0.15 mm shear, after which it remains relatively constant with a maximum variation of 0.65 mm. This abrupt aperture expansion highlights the role of local ∇z extrema, which force immediate dilation during minor shear displacement. Because synthetic surfaces lack these ∇z extrema, they exhibit a more gradual sliding behavior that underestimates initial dilation.

This abrupt $\bar{a}$ expansion significantly changes the $\hat{a}$ distribution, resulting in an increasing standard deviation $\sigma_{\hat{a}}$ with increasing shear in a range of 3% to 25% for the measured surface. Conversely, $\sigma_{\hat{a}}$ of the simulated surface remains nearly constant, with

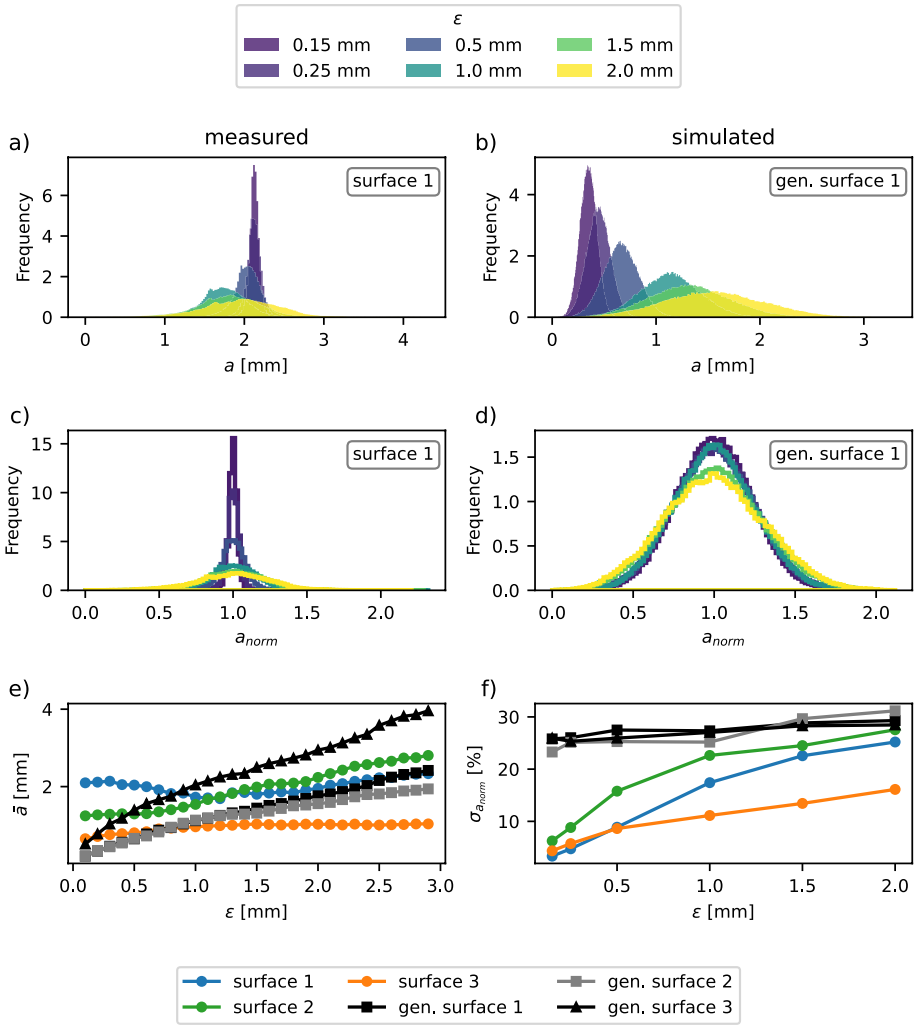


Fig. 6 Histograms of the local fracture aperture a for different shear distances ϵ for one measured roughness **(a)** and one simulated roughness **(b)** and histograms of the normalized mean aperture $\hat{a}$ of the histograms above **(c,d)**. For all rough surfaces the mean aperture $\bar{a}$ over ϵ**(e)** and the normalized aperture distribution width $\sigma_{\hat{a}}$ over ϵ**(f)**

a slight trend in the variation of below 4% across all shear distances. This stability in $\sigma_{\hat{a}}$ occurs because the shear-dependent increase in the distribution width is balanced by a proportional increase in the mean aperture. This balance is disrupted in natural surfaces by the presence of local roughness extrema. The summary of all investigated surfaces (Fig. 6e, f) confirms that these discrepancies represent a consistent characteristic across the entire dataset rather than isolated incidents. Specifically, none of the measured surfaces exhibit a steady increase in $\bar{a}$, whereas the simulated surfaces show a strong, shear-dependent increase. This steady growth in the simulated cases keeps $\sigma_{\hat{a}}$ constant, which contrasts with the increasing $\sigma_{\hat{a}}$ observed in the measured samples.

While the one-contact-point model can describe fracture aperture under low effective normal stress, experimental studies often focus on fractures under higher normal stress. There, the normal stress where mechanical deformation leads to the crushing of asperities, resulting in extended contact areas rather than a single contact point. To provide a more robust comparison, we simulated $\bar{a}$ with incrementally increased contact areas from a single point up to 20% for $\epsilon \leq 3$ mm (see Fig. 7) for the surface 1 and generated

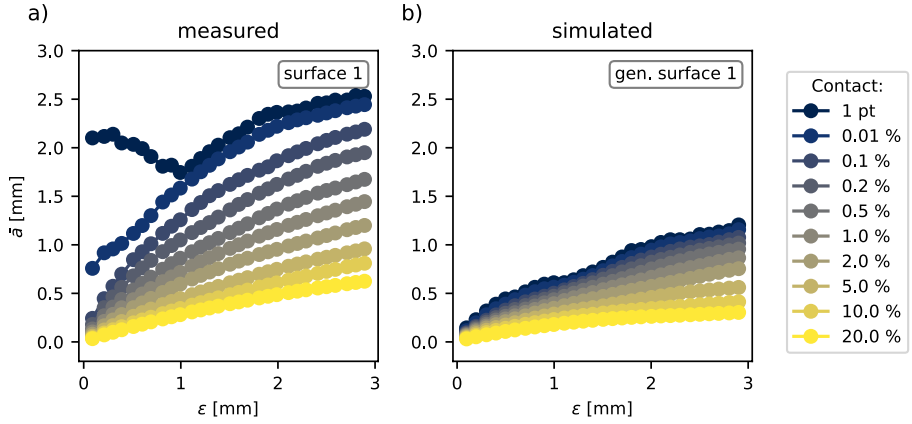


Fig. 7 The mean aperture $\bar{a}$ over shear distance ϵ for different contact areas for a measured surface **(a)** and a simulated surface **(b)**

surface 1. This method is related to the removal of roughness extrema since the contact happens first at the extreme ∇z positions. The results demonstrates that across the entire range of investigated contact areas, the measured fracture exhibits a higher $\bar{a}$ than the simulated fracture. Furthermore, the reduction of $\bar{a}$ for the surface 1 is more pronounced as the contact area increases than for the simulated surface. Although the rapid increase in $\bar{a}$, which exceeds 2 mm, for the measured surface is attenuated by increasing contact, the initial $\bar{a}$ remains higher for the measured surface across the entire analyzed range up to 20% contact area. Regarding shear, the contact model results in a steady increase in $\bar{a}$ for both surfaces. However, increasing the contact area leads to a 'smoothing' effect on this $\bar{a}$ increase. While the ∇z extrema are effectively removed by an increased contact area, $\bar{a}$ of the measured surface remains consistently higher. This suggests that the extrema are important with low contact models (contact area below 0.1% for the surface 1), but for larger contact areas also the ∇z distribution shape could be a reason for an increased $\bar{a}$. Overall, it indicates that simulated surfaces require a corresponding correction.

It is important to note that the normal aperture distribution in both investigated cases suggests a deviation from the log-normal distribution approach proposed by Renshaw (1995), where the hydraulic aperture is compared to the geometric mean of a. While the results from contact-area model appear more compatible with the log-normal model, this simplified approach tends to overestimate the presence of the smallest apertures when compared to the log-normal model (see Appendix B). It should be recalled that the current contact-area model neglects the influence of abrasion, which can lead to slickensides and the formation of gouge material that can block fluid pathways (Kalantar et al. 2025). While the steady increase in $\bar{a}$ and σ_a for the simulated fractures is well-documented in the literature, both for single-contact-point models (Marchand et al. 2020), and in comparison with normal pressure simulations (Cardona et al. 2021), the large a observed with only small ϵ represent a distinct geometric mechanism driven by ∇z extrema in the measured surfaces. These extrema result in an opening behavior functionally comparable to a normal opening of the simulated fracture (Appendix C). From a reservoir engineering perspective, this implies that conventional simulated surface models yield overly pessimistic predictions of slight-shear $\bar{a}$ enhancement. The similarity to normally opened fractures suggests that the hydraulic behavior of natural fractures

might be more accurately approximated in synthetic models by applying an additional normal displacement offset rather than relying on a single contact point or contact area alone. Since these geometric deviations redefine a, it becomes necessary to evaluate their subsequent impact on the fracture hydraulic behavior and spatial flow non-uniformity.

Effects on fracture flow

Differences in the fracture void geometry due to the roughness extrema strongly influence the flow within the fracture. The increased $\bar{a}$ has the most significant impact on fracture hydraulics. This influence can be quantified using the Cubic Law. The substantial differences for a 20 cm long fracture are visualized in Fig. 8a, showing that an $\bar{a}$ increase of approximately 2 mm leads to a reduction in Δp of over three orders of magnitude. In addition to this primary influence of the $\bar{a}$ increase, the σ_a further affects Δp, and modifies the flow uniformity with ϵ and $\bar{a}$.

Effects of the aperture distribution

The previous a analysis revealed a normal distribution for both simulated and measured surfaces, although $\sigma_{\hat{a}}$ increases exclusively for the measured surfaces with increasing ϵ . The influence of $\sigma_{\hat{a}}$ on the fracture pressure difference Δp is shown in Fig. 8c, d for the 1D LCL fracture flow. Here, local a_i values were randomly sampled from a normal distribution with defined widths, to isolate the effect of the a distribution width from $\bar{a}$ changes. A $\sigma_{\hat{a}} = 0$ corresponds to the parallel plate model. The resulting Δp values

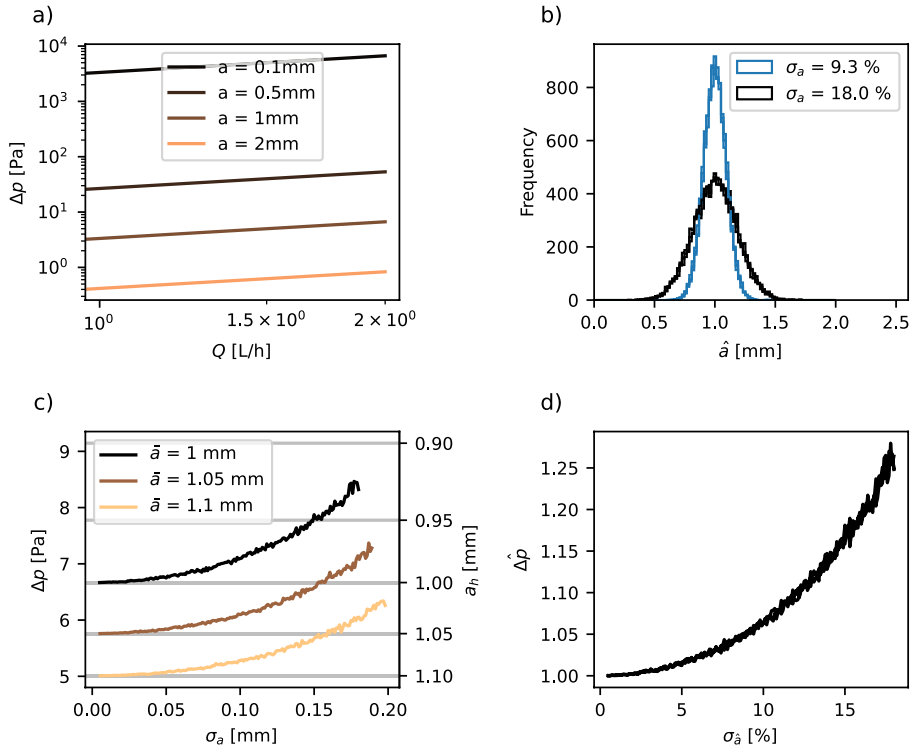


Fig. 8 Hydraulic differences with different apertures with the parallel plate simplification of a 20 cm x 20 cm fracture model at low flow rates (Q = 2 L/h corresponds to Re =2.78) **(a)**. Histogram of two exemplary normalized aperture $\hat{a} = a/\bar{a}$ distributions **(b)** chosen for the LCL calculations (Q = 2 L/h) shown in the bottom row: Hydraulics of three different $\bar{a}$ with varying local aperture distribution width σ_a **(c)** and the normalized pressure drop over the normalized aperture distribution width **(d)**

can be used to back-calculate the corresponding hydraulic aperture $\bar{a}_h$ (equal to a back calculation based on parallel plates), which is displayed on the second y-axis (Fig. 8c). The results reveal that Δp increases with $\sigma_{\hat{a}}$, with a slightly more pronounced increase for smaller $\bar{a}$. For example, compared to the $\sigma_a = 0$ case of $\bar{a}$ =1 mm, an increase to $\sigma_a = 0.15$ mm results in a Δp difference equivalent to a 5% reduction in $\bar{a}_h$. The influence of varying $\bar{a}$ can be eliminated by normalizing Δp by the parallel plate equivalent Δp_{pp} ($\sigma_{\hat{a}} = 0$) and using $\sigma_{\hat{a}}$. This normalization yields a unique relation between $\sigma_{\hat{a}}$ and the pressure ratio $\hat{\Delta p} = \Delta p / \Delta p_{pp}$, that remains valid regardless of Q and $\bar{a}$. The observed increase in Δp with a broadening a distribution is a direct consequence of the non-linear scaling of a in the LCL. Because Δp scales with a^{-3}, it is disproportionately governed by the lower tail of the a distribution. Essentially, the increased flow resistance in narrow segments outweighs the conductance gains in wider segments.

Consequently, the reduced $\sigma_{\hat{a}}$ observed in the measured surfaces provides a hydraulic advantage due to the reduction of bottlenecks. Because these simulations were conducted in two dimensions, the influence of these bottlenecks on flow resistance is amplified compared to three-dimensional fractures, where flow can bypass narrow passages (Brush and Thomson 2003). Combined with the overall increase in $\bar{a}$, this leads to a significantly lower Δp for natural fractures. The decreased Δp for the measured surfaces highlights a significant gap in current modeling: that $\sigma_{\hat{a}}$ is generally not accounted for in the correction or modification of the LCL. Instead, most existing corrections involve the calculation of effective or hydraulic apertures or incorporate $\sigma_{z,tot}$ (He et al. 2021). However, while $\sigma_{z,tot}$ is an insufficient parameter for characterizing self-affine fractures, other methods for calculating $\bar{a}_h$ from local apertures may only indirectly account for the effect of the aperture distribution, albeit by employing more computationally complex approaches. A systematic analysis of aperture distribution widths could eventually allow for a simpler correction factor, dependent on ϵ and ∇z extrema, to improve predictive accuracy.

Non-uniformity of fracture flow

To investigate the influence of the increased $\bar{a}$ on the local flow directions, we performed 3D simulations by analyzing the deviation of the flow direction from the mean flow direction θ. Figure 9a–d displays the height map of the applied surface, the a field of a sheared fracture case and the resulting flow directions for both a normal opening and the aforementioned sheared case. The statistical analysis of flow uniformity across various $\bar{a}$ and ϵ values is provided in Fig. 9e. In this context, $\bar{a}$ is varied to simulate different possible intensities of the roughness extrema, where high $\bar{a}$ occur at already slight shear.

The analysis reveals a normal distribution of θ with a mean predominantly centered at zero, validating the simulation given the no-flow conditions at the side walls. Minor shifts from the center at zero occur in sheared fractures, where a at the inlet and outlet is not constant along the y-axis. Given the normal distribution of θ, we utilized its standard deviation σ_θ as a metric for spatial flow non-uniformity. The results demonstrate that while non-uniformity remains constant during purely normal opening. However, in sheared fractures, the aperture plays a significant role regarding the flow direction by a reduction of σ_θ as $\bar{a}$ increases. In these cases, the increased $\bar{a}$, driven by the roughness extrema model, effectively opens bottleneck points. This reduces the necessity to divert around these narrow points, resulting in a more uniform flow field, thereby reducing the

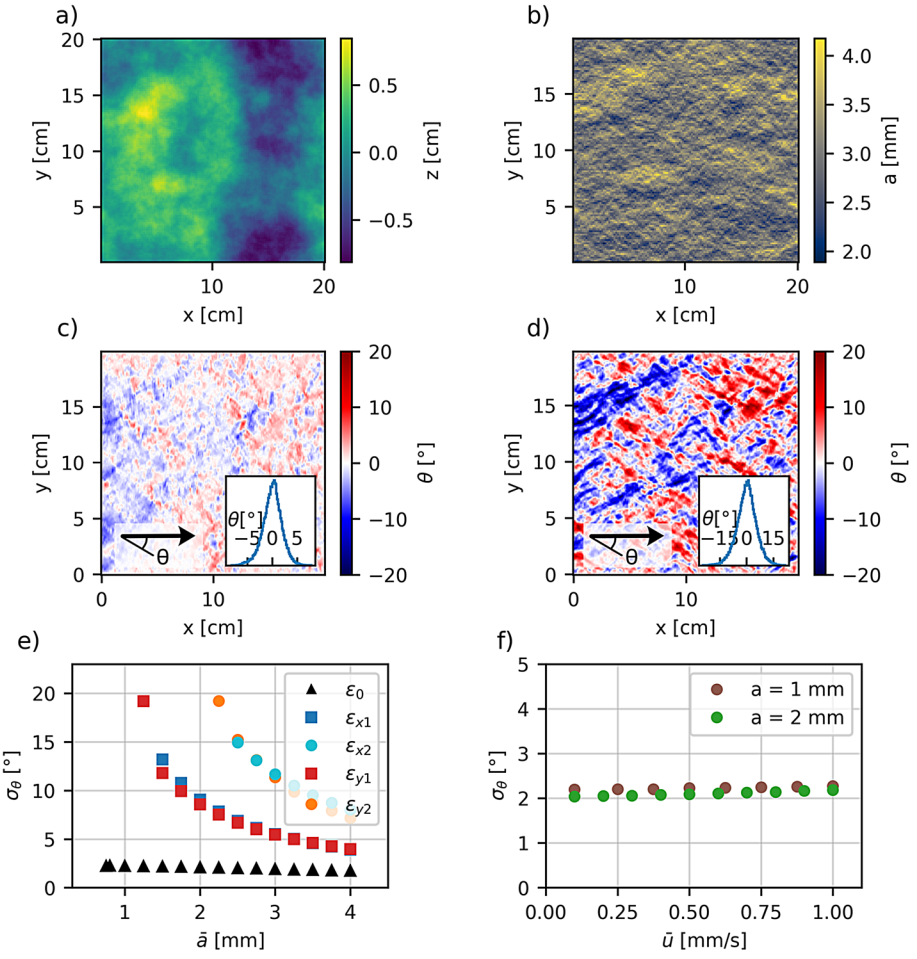


Fig. 9 Height map of the rough surface for the simulations **(a)**, aperture field of an example sheared surface (shear in y of $\epsilon_y = 1.56$ mm and $\bar{a} = 3$ mm) **(b)**, an exemplary flow direction θ distribution with the flow direction histogram as an inset for a normal opened fracture **(c)** and the sheared fracture of b **(d)**. The standard deviation of the flow direction σ_θ as a parameter for the non-uniformity of the flow over the fracture aperture $\bar{a}$ **(e)** without shear ϵ_0, a shear distance of 1.5625 mm for $\epsilon_{x1}, \epsilon_{y1}$ and a shear distance of 3.125 mm for $\epsilon_{x2}, \epsilon_{y2}$ **(e)** and the non-uniformity over different mean inflow velocities $\bar{u}$ without shear **(f)**

overall hydraulic tortuosity. Furthermore, a larger ϵ leads to a larger σ_θ for a constant $\bar{a}$, as the increased displacement creates additional narrow areas that force flow diversion. Notably, changes in the mean flow velocity $\bar{u}$ do not significantly affect σ_θ, indicating that the degree of spatial flow non-uniformity is primarily a geometric rather than a kinematic property in the investigated low flow rate regime.

Incorporating the impact of roughness extrema only through their effect on $\bar{a}$, rather than explicitly including them directly into the 3D mesh, this model enables a general study of spatial fracture flow non-uniformity across increasing $\bar{a}$ without requiring a specific definition of the extrema positions, amounts or magnitudes. However, the explicit inclusion of these extrema would lead to a slight increase in σ_θ (Appendix D), as the flow is forced to deviate around local contact points or closed areas. By quantifying spatial flow non-uniformity using σ_θ, we developed a continuous statistical approach. As all fracture flow simulations, this approach remains sensitive to the spatial resolution of the surface roughness. Consequently, applying higher-resolution roughness models or evaluating real rock fracture experiments will cause σ_θ to deviate from the values

presented here. Nevertheless, a qualitative comparison with the threshold-based models of different resolution can be performed by assuming that a higher σ_θ correlates with more pronounced channeling (see Appendix E for the foundation of this assumption). Thus, the observed increase of σ_θ with increasing ϵ is consistent with the shear-induced channeling increase reported by Marchand et al. (2020). While channeling studies suggest that the effect is strongly dependent on the shear direction (Egert et al. 2021), our σ_θ analysis shows no significant directional differences. This discrepancy may be caused by the artificial, physically often random threshold of channeling definitions. Such definitions potentially filter out below threshold flow channeling or directional changes that occur primarily during shear in the flow direction (ϵ_x). In deep geothermal reservoirs, these small-scale flow direction changes act as a geometric flow mixer. Such flow non-uniformity can result in increased tortuosity (see Appendix E). Its precise influence on fluid–rock heat transfer within fractured geothermal reservoirs remains under active investigation (Chen and Zhao 2020). Furthermore, the observed stability of σ_θ across varying $\bar{u}$ aligns with the constant degree of channeling found by Egert et al. (2023), confirming that topography, rather than $\bar{u}$, dominates flow paths.

Conclusion

This study evaluates the impact of local roughness extrema on the void geometry and hydraulic properties of granite fractures, demonstrating that they play a dominant role in governing fluid dynamics. To investigate the existence of these fracture roughness extrema, high-resolution topography measurements from three geologically diverse granite roughness samples were compared with synthetically generated self-affine surfaces. The overall sample roughness diversity was quantified using global and a local parameter. The explicit influence of the observed extrema in ∇z on the resulting fracture void geometry was evaluated by applying two aperture models. In a final step, the subsequent impact of the $\bar{a}$ increase on laminar fracture flow was simulated using both 1D and 3D numerical approaches to independently quantify the influence on fracture hydraulics and flow uniformity. Based on the results, the following key conclusions can be drawn:

- The results indicate that ∇z extrema constitute a general and potential universal feature of natural granite fracture roughness. The studied conventional roughness simulations systematically underestimate these ∇z extrema as their maximum-to-median ratio is one order of magnitude smaller. This underestimation has critical geometric consequences, as it leads to significantly lower $\bar{a}$ (up to 2 mm lower) and increased $\sigma_{\hat{a}}$ of above 20% for simulated surfaces. To adapt these theoretical models to the physical measurements, we suggest introducing an additional normal opening offset for the simulated surfaces. Such a $\bar{a}$ correction allows for a more realistic representation of the fracture void without a restrictive contact point, thereby more closely resembling natural systems driven by physical ∇z extrema.
- The resulting extrema-induced increase in $\bar{a}$ and decrease in $\sigma_{\hat{a}}$ reduce the hydraulic resistance of the fracture. While the increase in $\bar{a}$ is the primary factor defining the order of magnitude of the pressure drop, the local a distribution remains highly influential. Specifically, as shown within the LCL calculations, an increased $\sigma_{\hat{a}}$ of 18% leads to a pressure drop increase of over 25% compared to the parallel-plate approximation. This $\bar{a}, \sigma_{\hat{a}}$ sensitivity should be accounted for when modeling

fractured granitic reservoirs, either by applying a normal opening offset to simulate the found dilation or integrating geometry-based correction factors into LCL calculations.

- Flow non-uniformity is reduced in sheared fractures due to an increased mean aperture. Specifically, 3D flow simulations of a slightly sheared fracture demonstrate that an increase in $\bar{a}$ from 1.2 mm to 4 mm leads to a spatial flow non-uniformity reduction by 80%, resulting in a larger effective fluid-rock contact area for the main flow rate (90% of the flow). Consequently, accounting for this reduced channeling behavior in numerical models may be of interest for refining predictions of heat transfer and heat-extraction efficiency in deep geothermal applications.

To prove the universality of these roughness extrema and establish a reliable and generalized value for the proposed additional fracture opening offset, the local roughness extrema must be analyzed statistically using a larger sample size that includes an even wider variety of fracture origins and lithologies. Building on this, advancing synthetic surface generation algorithms will require a detailed analysis of the spatial distribution, shape, and enclosure of roughness extrema to determine whether they exist as isolated spots or are embedded within broader geometric patterns. Beyond refining these algorithms to produce more realistic generated surfaces, future work must also focus on verifying classical theoretical contact models against real fracture measurements, moving beyond regular geometries to account for the complex, irregular contact clusters observed in natural self-affine surfaces. In addition, the relevance of these extrema should be investigated at higher flow rates and validated at the field scale. This could be tested in underground research laboratories, such as the upcoming *GeoLaB*. Once operational, this facility is expected to provide the conditions required to measure fracture apertures, hydraulic conductivity, and heat transfer in situ.

Appendix A Extended sample analysis of local roughness extrema

To assess the robustness of the ∇z extrema pattern observed in the three natural granite samples discussed in Sect. "Influence of local topography on fracture void geometry", we conducted additional high-resolution topography measurements on further granite fracture surfaces. These supplementary samples were obtained from the same three geological formations as the primary dataset: Soultz-sous-Forêts (4 samples), Malsburg Granite (3 samples), and Tromm Massif (8 samples). Additionally, two sandstone samples from Soultz-sous-Forêts were analyzed to strengthen the hypothesis that roughness extrema are a universal feature of fracture surfaces.

Due to practical constraints across multiple measurement campaigns, the additional samples were acquired with varying spatial resolutions (Δx ranging from 20 μm to 30 μm) and scanned areas (3.05 cm^2 to 42 cm^2). This heterogeneity in measurement parameters prohibits direct comparison of absolute ∇z magnitudes across all samples. However, the maximum-to-median ratio ($\max(\nabla z)/\text{median}(\nabla z)$) over Δx serves as a metric that remains suitable for cross-sample comparison, as demonstrated in Fig. 5g and extended here in Fig. 10. The supplementary sandstone samples suggest that roughness extrema may represent a general characteristic of rough rock fractures. However, a larger sample size and greater lithological diversity are required to validate this hypothesis.

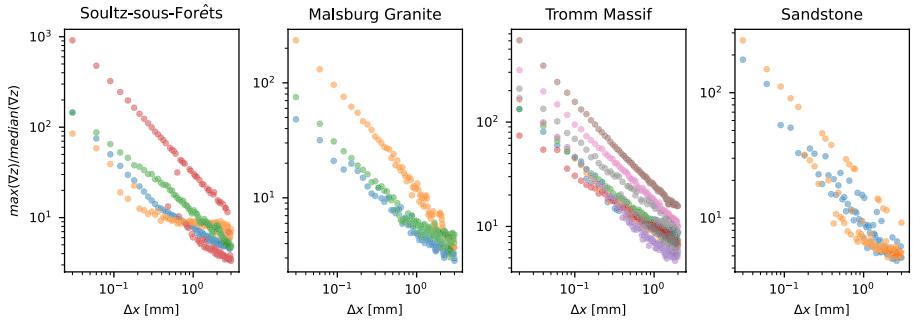


Fig. 10 Maximum-to-median local roughness gradient ratio (max(∇z)/median(∇z)) as a function of grid resolution Δx

Appendix B Aperture distribution with contact area

The contact model employed for the aperture analysis with a specified contact area neglects contact points for the calculation of the local aperture. This assumption introduces a cut-off effect in the local aperture a distribution. In Fig. 11 the histograms of a are plotted for one measured surface and one simulated surface. As the contact area increases, the normal distribution shifts toward lower mean apertures $\bar{a}$. The smallest a values are cut off, while the remaining distribution keeps its original shape, albeit shifted.

If it is assumed that physical measurements may result in lower small a, the resulting truncated a distributions become superficially comparable to the log-normal distributions found by Renshaw (Renshaw 1995) and others. This underestimation could possibly be due to experimental measurement uncertainties at small a or it could be physically more correct due to gouge material blocking the small aperture areas, leading to closure instead of narrow a.

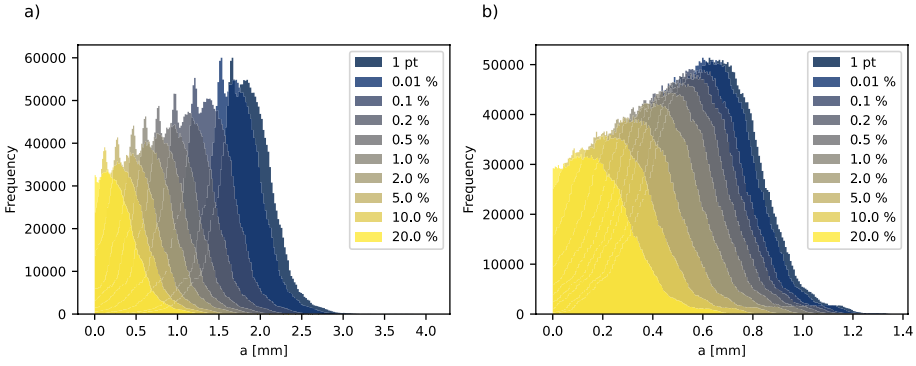


Fig. 11 Histograms of the local aperture a for different contact areas with shear of $\epsilon_x = 1.1$ mm for the surface 1 roughness (left) and the generated surface 1 (right)

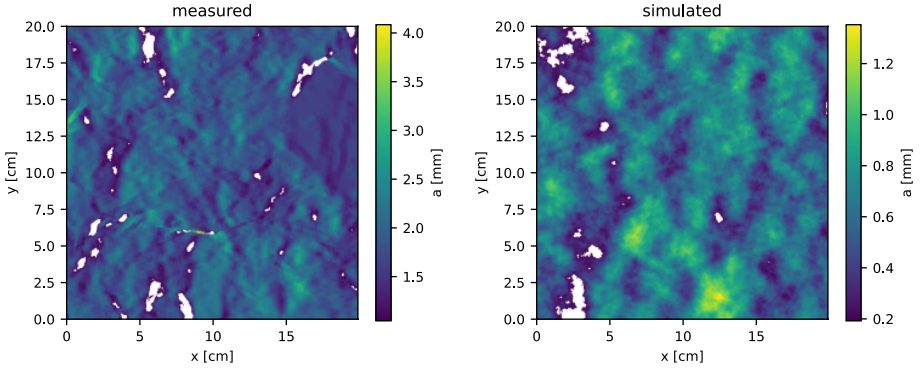


Fig. 12 Aperture maps for the measured surface 1 and generated surface 1 for the contact model with the white spots as contact area

The complexity of a detailed analysis of contact areas can be seen in Fig. 12 of an exemplary case with a 1.8% contact area and a shear displacement of 1.1 mm along x. The contact areas vary in size and are non-uniformly distributed across the fracture plane. In the measured surface, contact areas appear more elongated than in the simulated surface. Furthermore, the regions surrounding contact areas exhibit a more gradual aperture increase in the simulated surface fracture. These detailed morphological discrepancies complicate the formulation of a reliable contact model. Although numerous theoretical attempts have been made to analyze the impact of contact areas on fracture flow (Zimmerman et al. 1992), contact topology of self-affine fractures (Kottwitz et al. 2020) including rock sample measurements (Pirzada et al. 2021) remains an active subject of investigation, also concerning changes during fracture alteration (Deng et al. 2018).

Appendix C Simulated joint fracture

We assumed the occurrence of the normalized aperture distribution $\sigma_{\hat{a}}$ widening of the measured surface to be caused by the rapid increase in $\bar{a}$ observed at slight shear. We used the generated surface 1 to validate the hypothesis that the same result can be modeled by a wider normal opening of a simulated fracture. To test this, we calculated the aperture distribution under slight shear but with increasing normal aperture (Fig. 13). The resulting $\hat{a}$ distributions are comparable to those of the measured surfaces: The behavior observed in the simulated joint with decreasing normal $\bar{a}$ corresponds to the widening behavior of the measured surfaces with increasing shear. This verifies the validity of using simulated surfaces with additional normal aperture as an analog model for the measured a distribution.

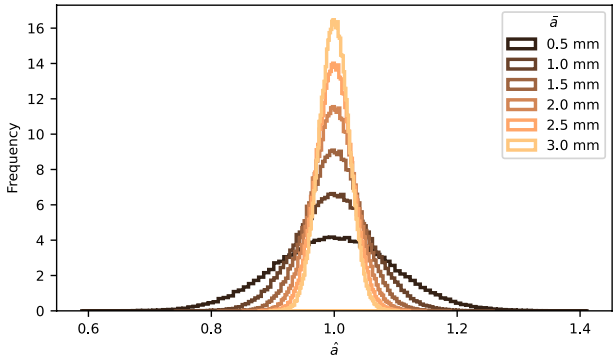


Fig. 13 Normalized aperture distribution with slight shear of $\epsilon_x = 0.15$ mm and joint simulated higher average apertures $\bar{a}$

Appendix D Flow with roughness extrema contact point

For simplification, the investigation of the flow direction was performed using the generated surface 1. Utilizing a simulated surface allowed for the modeling of low $\bar{a}$ without contact points as the measured surfaces. However, a normal opening of the original simulated surface neglects the local roughness extrema, leading to a contact point for the measured surfaces. To examine the flow distribution influenced by a contact point, the surface mesh was adapted to include a single contact point in the center of the surface. This contact point was modeled using two half-cones: the front half-cone (along the x-direction) was subtracted from the roughness profile, while the downstream half-cone was added to the rough surface. For the upper surface, the cones were shifted by one node in positive x-direction (Fig. 14 top-row). The half-cones were designed with a height nearly equal to half the aperture, leaving a negligible gap of 0.01 mm between the fracture walls. The cone radius spanned 5 surface nodes.

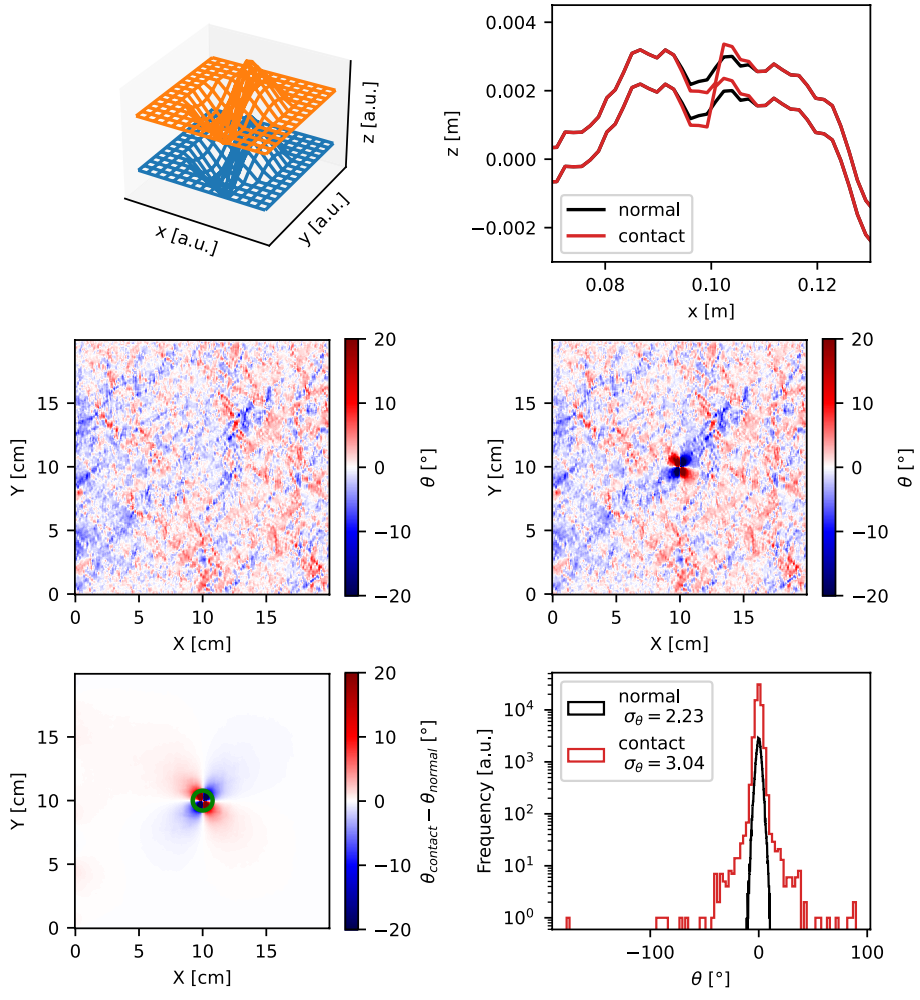


Fig. 14 Modification cone added to the normally opened simulated fracture (top-left) and the resulting surface height along x, in the main flow direction, at the center (top-right). The local flow direction θ within the normally opened fracture of the original *SAFFT* fracture (middle-left), θ of the locally modificated fracture with a contact point (middle-right), and the difference in flow direction between the two models (bottom-left) with the modification cone extend indicated by the green circle. Additionally, the histogram of θ with the standard deviation within the legend (bottom-right)

The resulting flow directions are visualized in Fig. 14 (middle row) for the original surface as well as the 5-node cone manipulation. The resulting histogram of flow directions θ is plotted in the bottom-right. The θ distribution widens significantly with a limited number of frequencies. This broadening is expected, as the fluid must divert around the nearly closed contact point. However, the strongly increased θ occur only within a localized area, leaving the flow in much of the fracture mainly undisturbed. Compared to the high θ standard deviations up to 20 ° with shear, the deviation of below 1° for the contact-point seem to be negligibly small. Consequently, we consider the normally opened simulated surface as a decent model for the measured surfaces with a roughness extrema contact point.

Appendix E Relation of σ_θ with channeling and tortuosity

For comparison with existing literature the found flow non-uniformity σ_θ was compared with the channeling effect and average stream path length.

To evaluate the correlation with flow channeling, we implemented the formulation used by Cardona et al. (2021) which quantifies the area in the $x-y$ plane responsible for 90% of the total flow rate $A_{90\%}$. Within this framework, a smaller area represents enhanced channeling.

Tortuosity was evaluated by analyzing the average path length of massless particles passing through the fracture. Streamline trajectories were calculated by numerically integrating the 3D velocity field using PyVista's streamlines_from_source filter (RK45, Sullivan and Kaszynski 2019). The seed positions were placed at the x, y cell centers of the inlet layer at the vertical (z) midpoint of the fracture.

The results in Fig. 15 demonstrates that the flow non-uniformity correlates with both $A_{90\%}$ and the path length. In prior literature (Egert et al. 2023), channeling was found to strongly depend on the shear direction, a finding consistent with our channel calculations. As shown in Fig. 15 left, the correlation between σ_θ and $A_{90\%}$ is primarily governed by the shear direction rather than the shear distance. Although σ_θ and $A_{90\%}$ are dominated by the shear direction and less by the shear distance. Besides ϵ_0, ϵ_x, ϵ_y all exhibit increased channeling (indicated by a decreasing $A_{90\%}$) with greater flow non-uniformity, their distinct groupings and inherent variability restrict this correlation to a qualitative assessment at this point. The average path length is strictly increasing with σ_θ (Fig. 15 right) and appears to be independent of the shear direction. However, normally opened

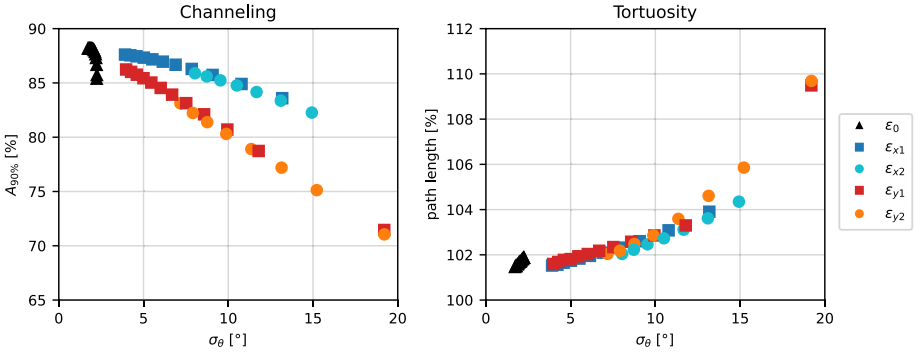


Fig. 15 3D simulation data of the flow non-uniformity relation to channeling and tortuosity. As a channeling parameter the x-y plane area $A_{90\%}$ is used and for the tortuosity the average path length relative to the fracture length in *x*

fractures display a different correlation trend compared to sheared fractures. Overall, it can be qualitatively concluded that a higher σ_θ corresponds to enhanced channeling (within one shearing direction) and increased streamline path lengths. Developing a precise quantitative metric to convert between these parameters remains beyond the scope of this study.

Acknowledgements
The authors want to thank the "Deutsche Forschungsgemeinschaft" (DFG) for granting the 'F4aT'-project. This study is part of the subtopic "Geoenergy" in the program "MTET—Materials and Technologies for the Energy Transition" of the Helmholtz Association.

Author contributions
C.M.B.: Methodology, validation, formal analysis, investigation, writing—original draft, visualization; F.N.: writing—editing, supervision, project administration, funding acquisition; T.K.: writing—editing, project administration, funding acquisition.

Funding
Open Access funding enabled and organized by Projekt DEAL. This work was supported by the "Deutsche Forschungsgemeinschaft" (DFG)—grant INST121384/201–1.

Data availability
Data sets generated during the current study are available from the corresponding author upon reasonable request.

Declarations

Competing interests
The authors declare no competing interests.

Received: 16 July 2026 / Accepted: 12 October 2026
Published online: 03 November 2026

References

Amitrano D, Schmittbuhl J. Fracture roughness and gouge distribution of a granite shear band. J Geophys Res Solid Earth. 2002. https://doi.org/10.1029/2002JB001761
Auradou H, Drazer G, Boschan A, et al. Flow channeling in a single fracture induced by shear displacement. Geothermics. 2006;35(5–6):576–88. https://doi.org/10.1016/j.geothermics.2006.11.004.
Beeler NM. On the scale-dependence of fault surface roughness. J Geophys Res Solid Earth. 2023;128(2):e2022JB024856. https://doi.org/10.1029/2022JB024856
Brush DJ, Thomson NR. Fluid flow in synthetic rough-walled fractures: navier-stokes, stokes, and local cubic law simulations. Water Resour Res. 2003;39(4):2002WR001346. https://doi.org/10.1029/2002WR001346.
Buness CM, Nitschke F, Kohl T. Implementation and validation of the F4aT laboratory for flow in rough fractures. Sci Rep. 2026;16(1):1956. https://doi.org/10.1038/s41598-025-34648-2.
Candela T, Renard F, Klinger Y, et al. Roughness of fault surfaces over nine decades of length scales. J Geophys Res Solid Earth. 2012;117(B8):2011JB009041. https://doi.org/10.1029/2011JB009041.
Cardona A, Finkbeiner T, Santamarina JC. Natural rock fractures: from aperture to fluid flow. Rock Mech Rock Eng. 2021;54(11):5827–44. https://doi.org/10.1007/s00603-021-02565-1.
Chen Y, Zhao Z. Heat transfer in a 3D rough rock fracture with heterogeneous apertures. Int J Rock Mech Min Sci. 2020;134:104445. https://doi.org/10.1016/j.ijrmms.2020.104445.
Deng H, Steefel C, Molins S, et al. Fracture evolution in multimineral systems: the role of mineral composition, flow rate, and fracture aperture heterogeneity. ACS Earth Space Chem. 2018;2(2):112–24. https://doi.org/10.1021/acsearthspacechem.7b00130.
Egert R, Nitschke F, Gholami Korzani M, et al. Stochastic 3D navier-stokes flow in self-affine fracture geometries controlled by anisotropy and channeling. Geophys Res Lett. 2021;48(9):e2020GL092138. https://doi.org/10.1029/2020GL092138.
Egert R, Nitschke F, Gholami Korzani M, et al. Spatial characterization of channeling in sheared rough-walled fractures in the transition to nonlinear fluid flow. Water Resour Res. 2023;59(10):e2022WR034362. https://doi.org/10.1029/2022WR034362.
Finenko M, Konietzky H. Numerical simulation of turbulent fluid flow in rough rock fracture: 3D case. Rock Mech Rock Eng. 2024;57(4):2297–323. https://doi.org/10.1007/s00603-023-03634-3.
Frérot L, Anciaux G, Rey V, et al. Tamaas: a library for elastic-plastic contact of periodic rough surfaces. J Open Source Softw. 2020;5(51):2121. https://doi.org/10.21105/joss.02121.
He X, Sinan M, Kwak H, et al. A corrected cubic law for single-phase laminar flow through rough-walled fractures. Adv Water Resour. 2021;154:103984. https://doi.org/10.1016/j.advwatres.2021.103984.
Hofmann H, Blöcher G, Milsch H, et al. Transmissivity of aligned and displaced tensile fractures in granitic rocks during cyclic loading. Int J Rock Mech Min Sci. 2016;87:69–84. https://doi.org/10.1016/j.ijrmms.2016.05.011.
Kalantar A, Hofmann H, Ji Y, et al. Limits of self-propping in enhanced geothermal systems: new experimental insights from shear, tensile and saw-cut fractures in Odenwald Granodiorite. J Geophys Res Solid Earth. 2025;130(10):e2025JB031938. https://doi.org/10.1029/2025JB031938

Kottwitz MO, Popov AA, Baumann TS, et al. The hydraulic efficiency of single fractures: Correcting the cubic law parameterization for self-affine surface roughness and fracture closure. Solid Earth. 2020;11(3):947–57. https://doi.org/10.5194/se-11-947-2020.
Li D, Wu Y, Hao Y, et al. Competitive roles of contact ratio and aperture in nonlinear flow transition through stressed three-dimensional rough fractures. Phys Fluids. 2026a;38(2):026604. https://doi.org/10.1063/5.0311854.
Li D, Wu Y, Hao Y, et al. Impact of local aperture reduction characteristics on nonlinear flow behavior in rough fractures. Geoenergy Sci Eng. 2026b;258:214306. https://doi.org/10.1016/j.geoen.2025.214306.
Marchand S, Mersch O, Selzer M, et al. A stochastic study of flow anisotropy and channelling in open rough fractures. Rock Mech Rock Eng. 2020;53(1):233–49. https://doi.org/10.1007/s00603-019-01907-4.
Méheust Y, Schmittbuhl J. Geometrical heterogeneities and permeability anisotropy of rough fractures. J Geophys Res Solid Earth. 2001;106(B2):2089–102. https://doi.org/10.1029/2000JB900306.
Mottl D. Hurst. GitHub repository. Available at https://github.com/Mottl/hurst. Accessed 14 Nov 2022
Nemoto K, Watanabe N, Hirano N, et al. Direct measurement of contact area and stress dependence of anisotropic flow through rock fracture with heterogeneous aperture distribution. Earth Planet Sci Lett. 2009;281(1–2):81–7. https://doi.org/10.1016/j.epsl.2009.02.005.
Park JW, Song JJ. Numerical method for the determination of contact areas of a rock joint under normal and shear loads. Int J Rock Mech Min Sci. 2013;58:8–22. https://doi.org/10.1016/j.ijrmms.2012.10.001.
Pirzada M, Bahaaddini M, Moradian O, et al. Evolution of contact area and aperture during the shearing process of natural rock fractures. Eng Geol. 2021;291:106236. https://doi.org/10.1016/j.enggeo.2021.106236.
Re F, Scavia C. Determination of contact areas in rock joints by X-ray computer tomography. Int J Rock Mech Min Sci. 1999;36(7):883–90. https://doi.org/10.1016/S0148-9062(99)00056-X.
Renshaw CE. On the relationship between mechanical and hydraulic apertures in rough-walled fractures. J Geophys Res Solid Earth. 1995;100(B12):24629–36. https://doi.org/10.1029/95JB02159.
Rong G, Cheng L, He R, et al. Investigation of critical non-linear flow behavior for fractures with different degrees of fractal roughness. Comput Geotech. 2021;133:104065. https://doi.org/10.1016/j.compgeo.2021.104065.
Schmittbuhl J, Gentier S, Roux S. Field measurements of the roughness of fault surfaces. Geophys Res Lett. 1993;20(8):639–41. https://doi.org/10.1029/93GL00170.
Sullivan C, Kaszynski A. PyVista: 3D plotting and mesh analysis through a streamlined interface for the Visualization Toolkit (VTK). J Open Source Softw. 2019;4(37):1450. https://doi.org/10.21105/joss.01450.
Zeng F, Cheng X, Guo J, et al. Effect of fluid penetration on tensile failure during fracturing of an open-hole wellbore. J Geophys Eng. 2018;15(3):952–61. https://doi.org/10.1088/1742-2140/aaa91f.
Zhu N, Yu Q. Temporal evolution of fracture transport properties of fractured shales during long-term stress compaction. Eng Geol. 2024;339:107663. https://doi.org/10.1016/j.enggeo.2024.107663.
Zimmerman RW, Paluszny A. Fluid Flow in Fractured Rocks. Hoboken, NJ: Wiley; 2024.
Zimmerman RW, Chen DW, Cook NG. The effect of contact area on the permeability of fractures. J Hydrol. 1992;139(1–4):79–96. https://doi.org/10.1016/0022-1694(92)90196-3.

Publisher's Note

Springer Nature remains neutral with regard to jurisdictional claims in published maps and institutional affiliations.